Interfacial CO_2-Mediated Nanoscale Oil Transport: from Impediment to Enhancement

Do Yoon Moh,[1] Chao Fang,[1,†] Xiaolong Yin,[2] and Rui Qiao[1,*]

[1] Department of Mechanical Engineering, Virginia Tech, Blacksburg, VA 24061, USA

[2] Petroleum Engineering Department, Colorado School of Mines, Golden, CO 80401, USA

Abstract. CO_2-based enhanced oil recovery is widely practiced. The current understanding of its mechanisms largely focuses on bulk phenomena such as achieving miscibility or reducing oil density and viscosity. Using molecular dynamics simulations, we show that CO_2 adsorption on calcite surfaces impedes decane transport at moderate adsorption density but enhances decane transport when CO_2 adsorption approaches surface saturation. These effects change the decane permeability through 8 nm-wide pores by up to 30% and become negligible only in pores wider than several tens of nanometers. The strongly nonlinear, non-monotonic dependence of decane permeability on CO_2 adsorption is traced to CO_2's modulation of long-chain hydrocarbon's interfacial structure, and thus the slippage between interfacial hydrocarbon layers and between interfacial CO_2 and hydrocarbon layers. These results highlight the new and critical role of CO_2-induced interfacial effects in influencing oil recovery from unconventional reservoirs, whose porosity is dominated by nanopores.

Table of Contents Entry

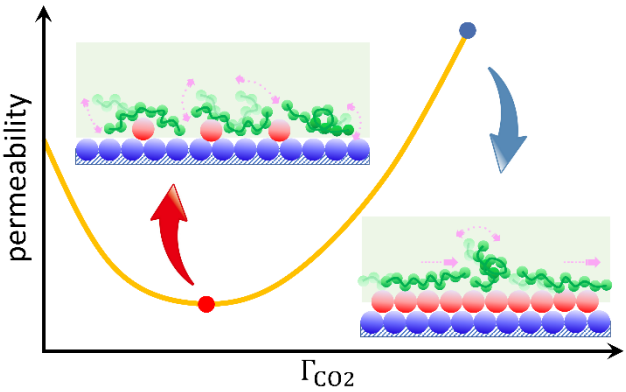

Sentence: CO_2 adsorption regulates the decane transport in inorganic nanopores by modulating the interlay mixing of interfacial fluids.

* To whom correspondence should be addressed. Email: ruiqiao@vt.edu

† Present address: Department of Chemical and Biomolecular Engineering, University of California, Berkeley.

1. Introduction

Enhanced oil recovery is widely practiced in hydrocarbon extraction operations. In particular, in unconventional reservoirs, where the decline of primary recovery rate is often rapid, implementation of enhanced recovery technologies helps offset the rapid decline of production rate and is crucial to the economical operation of these reservoirs.[1] Among the many enhanced recovery technologies, carbon dioxide (CO_2) injection is a popular approach and has shown considerable efficacy in unconventional reservoirs.[2-4] Nevertheless, the optimal practice of CO_2 injection remains challenging as evident from the mixed outcome in different reservoirs.[5] Resolving this challenge necessitates a fundamental understanding of the mechanisms of enhanced recovery by CO_2.

Many mechanisms have been suggested for the enhanced oil recovery by CO_2 injection. A majority of these mechanisms trace the enhanced recovery to the change of bulk properties of oil by CO_2 (e.g., the reduction of oil's viscosity and density) or elimination of multiphase transport (e.g., achieving miscibility with oil through condensation / vaporization interactions during CO_2-oil displacement).[2] Recently, interfacial effects associated with CO_2 injection have drawn increasing attention. For example, by adsorbing on pore surfaces in porous formation, CO_2 can displace hydrocarbons of various chain length from the pore surfaces and thus enhance their recovery.[6-12] While some of these studies also clarified the diffusion of CO_2 adsorbed on pore walls,[7, 10, 11] how the adsorbed CO_2 affects the transport of hydrocarbons, which is important for their recovery, has received much less attention[13, 14] and is not well understood.

Adsorbed CO_2 can potentially affect the transport of oil in unconventional reservoirs greatly. A hallmark of unconventional reservoirs is that their porosity is dominated by nanoscale pores.[15, 16] In nanoscale pores, interfacial interactions can significantly change the transport behavior due to the enormous surface-to-volume ratio. These interactions have been shown to lead to peculiar transport behavior, e.g., giant electrokinetic flow and amplified thermo-osmosis,[17-19] and classical theories can fail to describe the fluid transport in such pores quantitatively.[20, 21] Because adsorbed CO_2 molecules modify the interactions between the oil and the pore walls, they likely will also modulate oil transport in nanopores of unconventional reservoirs. Indeed, recent experimental study of permeation of decane-heptadecane (C_{10}-C_{17}) mixture through tight Niobrara core samples (pore throat size: 4-60 nm) already showed that CO_2 adsorbed on pore walls markedly changed the ratio of C_{10} and C_{17} in the liquids flowed through.[22]

In this work, we study the permeation of decane in calcite nanopores under different levels of CO_2 adsorption using molecular dynamics (MD) simulations. We show that decane permeation is impeded at modest adsorption density but enhanced at high adsorption density and these effects are important when pore is narrower than tens of nanometers. The molecular mechanisms of these effects are clarified.

2. Simulation System and Methods

System. In shales, oil was generated predominately in organic pores but some of the oil migrated to nearby layers dominated by inorganic pores over geological time scale (e.g., in some layers of Niobrara shales, a very significant portion of mineral is inorganic calcite and there is little kerogen).[22] Further, during oil production, some oil inevitably moves through inorganic pores to be recovered. Therefore, in this work we focus on inorganic pores. Previous studies showed that, in inorganic pores filled with hydrocarbons, CO_2 molecules form a distinct adsorption layer on their surfaces.[7, 9] To study how this adsorption layer affects oil transport, we adopt the simulation system shown in Fig. 1. The system features a slab of decane sandwiched between two calcite slabs and a layer of CO_2 molecules near each calcite slab. The center-to-center width of the pore (w) is 8.0 nm. Its accessible width (w_e) is smaller than w by 2δ due to the finite size of surface atoms and displacement of decane by CO_2 molecules (see below for definition of δ and Table S1 in the Supplementary Information for δ computed in different simulations). CO_2 molecules are confined near each calcite slab by a virtual graphene layer that interacts *only with CO_2 and not with decane*, and the oil between virtual graphene layers is free of CO_2. By properly positioning the graphene layers, they hardly affect the distribution of CO_2 molecules behind them (see Fig. S1) and exert little hindrance to the lateral motion of CO_2

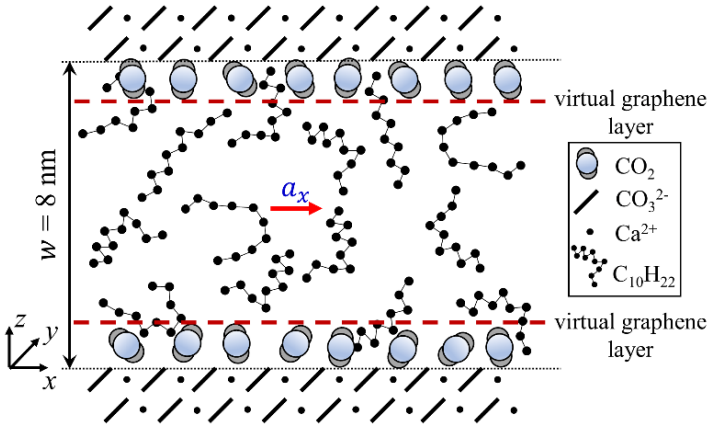

Fig. 1. A schematic of the simulation system for studying decane transport through slit calcite pores. Virtual graphene layers (red dashed lines) interacting only with CO_2 confine them near the calcite surface to ensure a well-defined CO_2 adsorption density during simulation. z = 0 corresponds to the uppermost oxygen atom layer of the lower calcite slab.

molecules due to their extremely smooth surface.[17] With this setup, we aim at revealing the essential physics of flow modulation by interfacial CO_2, unobscured by the modulation of bulk oil properties by CO_2. Furthermore, confining CO_2 at calcite-oil interfaces allows us to precisely maintain a CO_2 adsorption density (Γ_{co2}) on the calcite wall in each simulation, thus helping us systematically assess its impact on oil transport.

Molecular models. Each calcite slab is cut from a calcite crystal in the 1014 direction. The calcite slab measures 4.85×3.98 nm^2 in the lateral (*xy*-) plane and has six layers of atoms. For a given CO_2 adsorption density Γ_{co2}, which corresponds to a certain pressure of gaseous CO_2 in equilibrium with a calcite-decane interface (see Fig. S2), the corresponding number of CO_2 molecules are packed near each calcite surface. The number of decane molecules in the calcite pore is then adjusted iteratively so that the decane density at the center of the pore is within 0.5% of the bulk density of decane at 300 K and 1 bar. The virtual graphene layers are positioned at 0.70 nm from the innermost oxygen atoms of each calcite slab. The pore's center-to-center width w is measured between the innermost oxygen atoms of the two calcite slabs. The pore width accessible to decane is defined as $w_e = \int_0^w \rho_{c10}(z)dz\,/\bar{\rho}_b$, where ρ_{c10} and $\bar{\rho}_b$ are the decane density across the pore and the bulk decane density, respectively. The effective position of a calcite surface is thus located at $\delta = (w - w_e)/2$ in front of its nominal position set by its surface oxygen atom layer (see Fig. 1).

Decane is modeled using the OPLS-AA force fields with recently optimized parameter sets.[23] CO_2 is described using the TraPPE force fields.[24] The Lennar-Jones (LJ) parameters and partial charges of calcite atoms are taken from the re-fitted Dove's potential.[25] The calcite slabs are fixed in simulations. The LJ parameters between dissimilar atoms are obtained using the geometric combination rule.

Molecular methods. Simulations are performed using Gromacs 4.5.6.[26] The LJ potential is computed using direct summation with a cut-off length of 1.2 nm. Electrostatic interactions are computed using the Particle mesh Ewald (PME) method with a real space cutoff of 1.2 nm and an FFT spacing of 0.12 nm. Similar to most simulations of nanofluidic transport, to remove the periodicity in the *z*-direction, the simulation box height is set to 3 times of the pore width and the slab correction method is used together with the PME method.[27] After packing molecules into the system using the Packmol code,[28] each system is equilibrated first at 400 K and then at 300 K for 10 ns using a time step of 2 fs. A production run of 20 – 50 ns is then performed using a time step of 1 fs in the NVT ensemble. Temperature is controlled using the velocity rescaling thermostat with a time constant of 2 ps.

To compute the permeability of the pore for decane, an acceleration of $a_x = 1.4\times10^{-3}$ nm/ps^2 is applied in the x-direction. The permeability of the pore for decane is computed using $k = \dot{m}\bar{\mu}/\bar{\rho}^2 w_e a_x$, where $\dot{m}$ is computed by $\dot{m} = \int_0^w \rho_{c10}(z)u(z)dz$, and $\bar{\mu}$ is the viscosity of decane that is obtained by fitting the velocity profile in the central portion of the pore to a parabolic profile (see Fig. 3).

To predict decane transport in pores wider than 8.0 nm, we use the velocity embedding technique.[27, 29] This technique leverages the fact that the flow in these pores observes the Navier-Stokes equation except that the velocity slip at wall and non-bulk viscosity near wall must be considered.[30, 31] While these parameters can be extracted from MD velocity data, doing so requires velocity with very low noise as derivatives of velocity must be computed. The velocity embedding technique circumvents this difficulty by embedding the velocity in an interfacial region within a narrow pore into that within a wide pore.[27, 29] Specifically, the velocity in region within Δ from the wall of a wide pore is

$$u_w(z) = F(z)u_n(z) - \int_0^z \frac{dF}{ds}u_n(s)ds \quad (1)$$

where $u_n(z)$ is the fluid velocity in the same region inside the narrow (here, 8 nm-wide) pore and F is

$$F(z) = \frac{\int_{c_w}^z \rho_{c10}^w(z)a_x^w dz}{\int_{c_n}^z \rho_{c10}^n(z)a_x^n dz} \quad (2)$$

where c_w and c_n are the center of the wide and narrow pores, respectively. Superscripts "w" and "n" denote values in the wide and narrow pores, and variables in the narrow pore are obtained from MD simulations. The velocity profile in region Δ away from the wall is computed by solving the Stokes equation with bulk decane viscosity. The velocity at z = Δ obtained using Equation (1) is used as the boundary condition for this calculation. As an example, the decane velocity profile in a 15 nm-wide calcite pore with $\Gamma_{co2} = 5.12$ nm^{-2} computed from the velocity profile in an 8 nm-wide pore with the same Γ_{co2} is shown in Fig. S3 in the Supplementary Information.

3. Results and Discussion

Using the model in Fig. 1, we compute the permeability of calcite pores for decane at Γ_{co2} = 0, 1.28, 2.56, 3.85, 4.17, 4.49, 4.81, and 5.12 nm^{-2} by imposing a constant acceleration to decane molecules in the pore. Due to the strong affinity of CO_2 molecules to calcite, $\Gamma_{co2} = 4.49$ and 5.12 nm^{-2} correspond to the adsorption at calcite-decane interfaces in equilibrium with a pure-CO_2 environment having only a pressure of ~2.1 and 24.3 bar, respectively, at 300 K (see Fig. S2 in the Supplementary Information). The CO_2 pressure considered here is much lower than the CO_2 injection

pressure used in unconventional reservoirs (e.g., an injection pressure of 17-31 MPa is common).[32] However, as one moves away from the injection point and CO_2 diffuses into oil, the chemical potential or activity of CO_2 decreases (e.g., far away from the injection point, CO_2 concentration / activity is 0). Therefore, while the chemical potential of CO_2 presented by the low pressures considered in this study is not applicable near the injection point, it becomes relevant as the distance from the injection point increases.

Figure 2 shows the permeability of the 8 nm-wide pores relative to that at $\Gamma_{co2} = 0$. As Γ_{co2} increases from 0 to 2.56 nm^{-2}, the decane permeability decreases by ~30%. As Γ_{co2} increases, the permeability increases more and more rapidly. At $\Gamma_{co2} = 5.12\ nm^{-2}$, which is close to the saturation density of CO_2 in the first adsorption layer (~5.15 nm^{-2}), the permeability is 21% higher than that at $\Gamma_{co2} = 0$. The impediment and enhancement effects in narrower pores are expected to be stronger than those in the 8 nm-wide pores. To see how strong are these effects in wider pores, using the decane density and velocity profiles computed in the MD simulations, we compute the decane transport in wider pores using the velocity embedding technique (for a sample calculation, see Fig. S3 in the Supplementary Information).[27, 29] The predicted permeability for pores with a center-to-center width of 15-100 nm is shown in Fig. 2. We observe that the impediment (enhancement) of the decane transport at low (high) CO_2 adsorption density remains strong in 15 nm-wide pores, and these effects become less than 5% only in pores wider than about 30 nm.

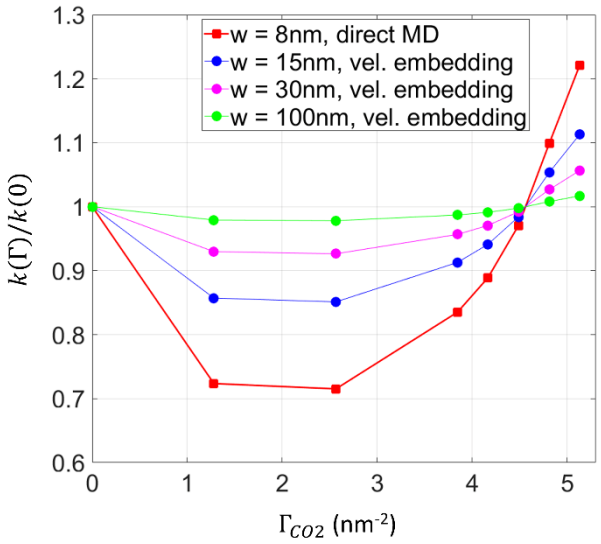

Fig. 2. Variation of the decane permeability of calcite slit pores at different CO_2 adsorption densities Γ_{co2} .

To understand the nonlinear, non-monotonic evolution of permeability with interfacial CO_2 density, we examine the distribution and transport of decane in the 8 nm-wide pores at different Γ_{co2}. Figure 3a

shows that, at $\Gamma_{co2} = 0$, the favorable interactions between decane and calcite leads to the formation of three decane layers near the calcite surface, and the first decane layer is especially well defined. When driven by an external force (in our simulations, an acceleration in the x-direction), the flow of decane exhibits a parabolic velocity profile at position ~1.0 nm away from the pore wall (see Fig. 3a), which is expected because the classical hydrodynamic model is expected to hold in this rather wide pore.[21, 30] Molecules within the first decane layer move almost concertedly as evident from the rather flat velocity profile in region $0 < z < 0.5$ nm. The collective velocity of these decane molecules is small because of their strong friction with the calcite surface. As we move further away from the calcite surface, a clear slippage between the first and second decane layer (see the red arrow in Fig. 3a) emerges. This interlayer slippage between neighboring decane layers, reminiscent of the dry slip in molecularly confined fluids,[33] leads to a rather large velocity of the second decane layer. This interlayer slippage is clear for the heavy (long-chain) hydrocarbons studied here and not often observed for monoatomic (or low molecular weight) fluids, and hence it highlights a new physics of conformation-induced interfacial slippage. Due to this slippage, although the first decane layer moves slowly, the *apparent* slip length at calcite surface, computed by extrapolating the fitted parabolic velocity profile in pore to the effective position of the pore wall ($z = \delta = 0.06$ nm), is only −0.10 nm.

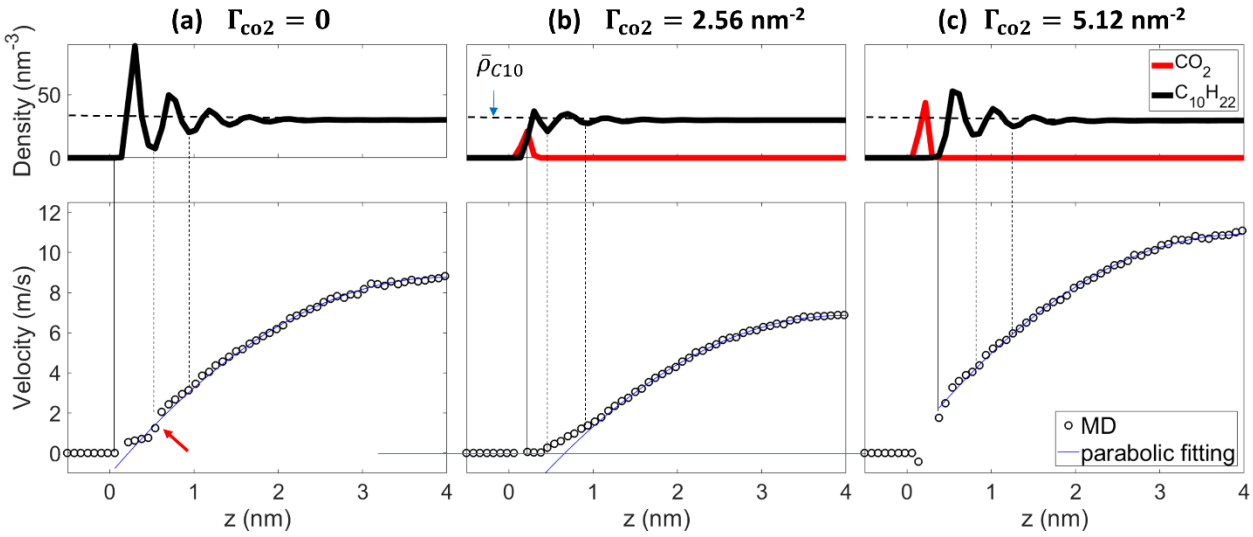

Fig. 3. The density and velocity profiles of the carbon atoms in decane across an 8.0 nm-wide calcite pore with a CO_2 adsorption density of $\Gamma_{co2} = 0$ (**a**), $\Gamma_{co2} = 2.56$ nm^{-2} (**b**), and $\Gamma_{co2} = 5.12$ nm^{-2} (**c**). Profiles are shown only in the pore's lower half because of symmetry. $z = 0$ corresponds to the innermost oxygen atoms of the calcite slab. The thin, black solid lines denote the effective position of calcite surface ($z = \delta$) defined in the text.

As the CO_2 adsorption density increases to $\Gamma_{co2} = 2.56$ nm^{-2}, a significant fraction of the molecules in the first decane layer is displaced from the calcite surface; beyond the first decane layer, layering becomes much weaker (see Fig. 3b). Figure 3b shows that the first decane/CO_2 layer is nearly

immobile and the interlayer slip between the first and second decane layer vanishes. Furthermore, the smaller curvature of the velocity profile in the space occupied by the second decane layer (0.46 nm $< z <$ 0.94 nm) than in bulk decane indicates that the local viscosity is higher than the bulk viscosity. These effects together reduce the velocity of decane in the interfacial region and, in turn, that in the entire pore. As such, the pore's permeability becomes smaller than that at $\Gamma_{co2} = 0$. This decrease of permeability is also manifested in the apparent slip length at calcite surface, which becomes −0.35 nm.

As the CO_2 adsorption density increases further to $\Gamma_{co2} = 5.12$ nm^{-2}, which is close to the saturation density of CO_2 on the calcite surface, decane molecules are mostly displaced from the calcite surface (see Fig. 3c). The decane molecules, however, form a conspicuous, new first layer centering on $z = 0.56$ nm, which in turn induces another modest layer at $z = 1.02$ nm. Figure 3c shows that a distinct slip occurs between the adsorbed CO_2 layer and the new first decane layer. Furthermore, the curvature of the velocity near the wall is similar to that in the bulk region, indicating that this first decane layer exchanges momentum with the bulk through a viscosity close to that of the bulk. Because of the emergence of interfacial slip and the bulk-like viscosity of interfacial decane, the velocity of the fluid molecules in the first decane layer, and thus that of the decane in the central portion of the pore, becomes much higher than those at $\Gamma_{co2} = 2.56$ nm^{-2}. As such, the permeability of decane through the pore increases greatly. The enhancement of transport is also manifested as a positive apparent slip length of 0.40 nm at the calcite-decane interface.

The above analysis shows that the impediment of oil transport at modest CO_2 adsorption density is mainly caused by the elimination of the interlayer slip between the interfacial decane layers, and the enhancement of oil transport at high CO_2 adsorption density is mainly caused by the emergence of slip between CO_2 and the first decane layer. To understand the mechanisms of these evolving slip behaviors at different CO_2 adsorption densities, we now examine the packing of decane and CO_2 molecules near the calcite surface.

Figure 4a shows top-view and side-view snapshots of representative decane molecules in the first layer of decane adsorbed on the calcite surface at $\Gamma_{co2} = 0$ (a decane molecule is taken to be in the first layer if one of its carbon atoms is within the first decane density peak, i.e., $0 < z <$ 0.54 nm). Decane molecules in this layer are usually highly stretched and mostly adopt a co-planar structure on the calcite surface, in excellent agreement with recent MD simulations by the Feng group.[10] A small fraction of decane molecules simultaneously belong to the second decane layer. However, mixing of decane between the first and the second layers is limited. To quantify this mixing, we compute an interlayer

mixing index M_i for each of the three decane layers near the calcite surface (i =1: $0 < z < 0.54$ nm; i = 2, $0.54 < z < 0.96$ nm; i = 3: $0.96 < z < 1.42$ nm, see Fig. 3a). Specifically, for each decane molecule in a layer i, an isolation parameter $\beta = 1$ is assigned if all its carbon atoms reside in the same layer; otherwise, an isolation parameter $\beta = 0$ is assigned. The interlayer mixing index of a layer i is $M_i = 1 - \bar{\beta}_i$, where $\bar{\beta}_i$ is the average of the isolation parameter of all decane molecules in this layer. $M_i = 0$ corresponds to the situation where all decane molecules in a layer i reside solely in this layer and thus this decane layer is not at all mixed with its neighbor layers. $M_i = 1$ corresponds to the situation where each decane molecule in a layer i extends to neighbor layers and thus this decane layer is well mixed with its neighbor decane layers.

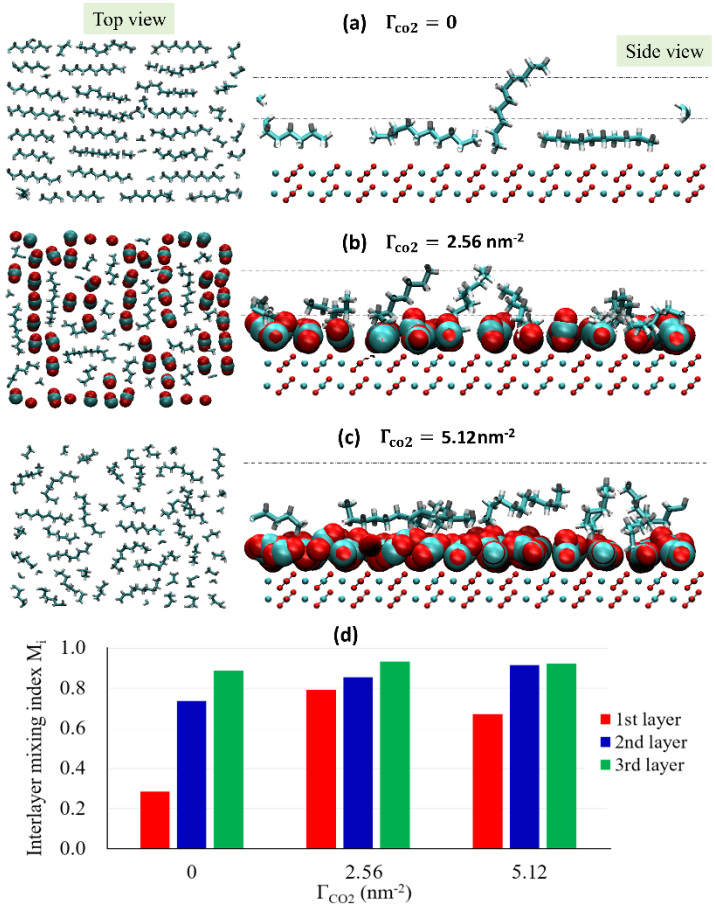

Fig. 4. (**a-c**) Snapshots of some representative decane molecules near the calcite surface at a CO_2 adsorption density of $\Gamma_{co2} = 0$ (a), 2.56 nm^{-2} (b), and 5.12 nm^{-2} (c). (**d**) The interlayer mixing index M_i of the first, second, and third interfacial decane layers near calcite surfaces with different CO_2 adsorption density. In (a-c), the two horizontal dashed lines denote the upper boundary of the first and second decane layer, which are defined based on the first and second valleys of the decane density profiles in Fig. 3.

Figure 4d shows that the interlayer mixing index of the first, second, and third decane layers near the calcite surface is 0.28, 0.73, and 0.89, respectively at $\Gamma_{co2} = 0$. The poor mixing of the first decane

layer with the two other layers helps explain the distinct slip between the first and second decane layer observed in Fig. 3a. This is akin to the observation that the hydrodynamic slippage at the interface between two immiscible liquids is strong when the mixing of the two types of molecules is poor in the interfacial zone.[34] The mixing of the second and third decane layers with their neighboring layers is much better, and thus the slip between the second and third decane layers is essentially absent (see Fig. 3a). A more detailed analysis of the distribution of carbon atoms of decane molecules in the three layers shows that some of the decane molecules in the second layer protrudes into the first decane layer (see Fig. S4), which explains why the average velocity of decane in the first layer is non-zero despite the intimate contact (and thus strong friction) between most of the decane molecules in this layer with the calcite surface.

As the adsorption density Γ_{co2} increases to 2.56 nm^{-2}, Fig. 4d shows that the mixing index of the first decane layer with its neighbor layers (M_1) increases from 0.28 to 0.8. The enhanced mixing of the first and second decane layers eliminates the slippage between them, which was observed at $\Gamma_{co2} = 0$. Meanwhile, because adsorbed CO_2 molecules adopt a non-coplanar configuration with respect to the calcite surface (see Fig. S5), decane molecules in the first layer can intercalate some of their carbon atoms into the CO_2 adsorption layer (also see Fig. S4) to mix with adsorbed CO_2 molecules. To quantify the mixing between the first decane layer and the CO_2 layer, we define a decane-CO_2 mixing index as $M_{d1\text{-}co2} = N_{d1,co2}/N_{d1}$ (N_{d1} is the number of decane molecules belonging to the first decane layer; $N_{d1,co2}$ is the number of decane molecules who not only belong to the first decane layer but also have at least one carbon atom residing in space occupied by the first CO_2 adsorption layer). At Γ_{CO2} = 2.56 nm^{-2}, $M_{d1\text{-}co2}$ is 0.85, indicating that the first decane layer is mixed well with the CO_2 layer, which helps eliminate the slippage between them. The CO_2 layer itself has a negligible streaming velocity due to the strong quadruple-dipole interactions with the calcite surface. It follows that the velocity of the first decane layer is very small. Overall, the elimination of slippage between interfacial decane layers and the absence of slippage between the interfacial decane and adsorbed CO_2 impede decane transport (see Fig. 3b), which help explain the lower decane permeation at $\Gamma_{co2} = 2.56$ nm^{-2} than at $\Gamma_{co2} = 0$.

As the adsorption density Γ_{co2} increases further to 5.12 nm^{-2}, Fig. 4d shows that the mixing of the first decane layer with its neighbor layer is reduced but still much stronger than that at $\Gamma_{co2} = 0$. As such, the interlayer slippage between the first and second decane layer remains suppressed. Meanwhile, because CO_2 adsorption on the calcite surface is close to the saturation limit (here, the tight packing of CO_2 molecules is partly facilitated by the fact that, compared to that at Γ_{co2} = 2.56 nm^{-2}, they align better with calcite surface's normal direction, see Fig. S5), little space is available on the calcite surface

for decane molecules to intercalate between adsorbed CO_2 molecules. Hence, the mixing between the first decane layer and the CO_2 adsorption layer is essentially absent (e.g., the decane-CO_2 mixing index $M_{d1\text{-}co2}$ is 0.02; see also Fig. 3c's bottom panel and Fig. S4c). Because of this poor mixing, a significant slippage emerges between the CO_2 layer and the first decane layer (see Fig. 3c), which causes decane permeation to increase greatly at $\Gamma_{CO2} = 5.12$ nm^{-2}.

Overall, modulation of decane permeation by CO_2 adsorption originates largely from modulation of the mixing between adsorbed CO_2 and the first interfacial decane layer. In this work, CO_2 molecules in the bulk are intentionally removed and the diffusion of CO_2 molecules out of the adsorption layer is blocked. In practice, CO_2 molecules adsorbed on a surface can exchange with those away from the surface and, even at modest CO_2 pressure, multilayer adsorption of CO_2 occurs. Therefore, it is useful to assess whether the mixing of the first CO_2 and decane layers is affected strongly by these phenomena. Here, we compute the decane-CO_2 mixing index $M_{d1\text{-}co2}$ in the system shown in Fig. S1, where a calcite-decane sub-system is in equilibrium with a CO_2 gas at a pressure of 24.3 bar. The density of the first CO_2 layer is determined to be $\Gamma_{CO2} = 5.12$ nm^{-2}. In this system, there is free exchange between CO_2 adsorbed on calcite surface and that in region away from the surface. Further, a second CO_2 density peak is visible from the CO_2 density profile (see Fig. S1c). $M_{d1\text{-}co2}$ is found to be 0.05 in this system. Therefore, the mixing of the first CO_2 and decane layers is slightly enhanced compared to the situation shown in Fig. 3c and 4c, where Γ_{CO2} is also 5.12 nm^{-2} and $M_{d1\text{-}co2}$ is 0.02. However, this enhancement is minor because 95% of decane molecules in the first decane layer still don't mix with the first CO_2 layer at all.

4. Conclusions

In summary, adsorption of CO_2 on calcite surfaces can either impede or enhance the permeability of decane through calcite pores, depending on the amount of CO_2 adsorbed. This modulation of decane transport by CO_2 adsorption is important in pores with width up to several tens of nanometers. Impediment of decane transport at modest CO_2 adsorption densities is attributed to suppression of the slippage between interfacial decane layers, which is caused by the enhanced interlayer mixing at modest CO_2 adsorption. Enhancement of decane transport at high CO_2 adsorption densities is attributed to the slippage between the interfacial CO_2 and decane layers, which emerges when decane is nearly completely displaced from the calcite surface by CO_2 molecules. These results highlight the role of CO_2 adsorption in controlling the interfacial structure of long-chain hydrocarbons and its complex influence over interfacial/interlayer slippage and hydrocarbon transport in narrow pores. These

interfacial effects, neglected in enhanced oil recovery theories for conventional reservoirs, should be considered in unconventional reservoirs dominated by nanoscale pores.

Acknowledgments. D.Y.M., C.F., and R.Q. gratefully acknowledge the allocation of computing time by the Advanced Research Computing office at Virginia Tech. The work at Virginia Tech is partially supported by the NSF under grant number CBET-1705287. X.Y. acknowledges the support of the Unconventional Reservoir Engineering Project consortium at the Colorado School of Mines.

References

1. L. Wang, Y. Tian, X. Y. Yu, C. Wang, B. W. Yao, S. H. Wang, P. H. Winterfeld, X. Wang, Z. Z. Yang, Y. H. Wang, J. Y. Cui and Y. S. Wu, *Fuel*, 2017, **210**, 425-445.
2. B. Jia, J. S. Tsau and R. Barati, *Fuel*, 2019, **236**, 404-427.
3. X. Zhou, Q. W. Yuan, X. L. Peng, F. H. Zeng and L. H. Zhang, *Fuel*, 2018, **215**, 813-824.
4. T. A. Siqueira, R. S. Iglesias and J. M. Ketzer, *Greenhouse Gases-Science and Technology*, 2017, **7**, 802-816.
5. J. J. Sheng, *Journal of Petroleum Science and Engineering*, 2017, **159**, 654-665.
6. H. Zhang and D. Cao, *Chem. Eng. Sci.*, 2016, **156**, 121-127.
7. R. Wang, F. Peng, K. Song, G. Feng and Z. Guo, *Fluid Phase Equilibria*, 2018, **467**, 25-32.
8. H. Sun, H. Zhao, N. Qi, X. Qi, K. Zhang, W. Sun and Y. Li, *RSC Adv.*, 2016, **6**, 104456-104462.
9. M. S. Santos, L. F. M. Franco, M. Castier and I. G. Economou, *Energy & Fuels*, 2018, **32**, 1934-1941.
10. F. Peng, K. Xiong, R. Wang, Y. Li, Z. Guo and G. Feng, *Energy & Fuels*, 2020, **34**, 2925-2935.
11. S. B. Badmos, T. Bui, A. Striolo and D. R. Cole, *J. Phys. Chem. C*, 2019, **123**, 23907-23918.
12. N. Choudhary, A. K. Narayanan Nair, M. F. A. Che Ruslan and S. Sun, *Scientific Reports*, 2019, **9**, 19784.
13. S. Wang, F. Javadpour and Q. Feng, *Fuel*, 2016, **181**, 741-758.
14. T. Fang, Y. Zhang, R. Ma, Y. Yan, C. Dai and J. Zhang, *Applied Surface Science*, 2019, **494**, 80-86.
15. G. R. Chalmers, R. M. Bustin and I. M. Power, *Am. Assoc. Pet. Geol. Bull.*, 2012, **96**, 1099-1119.
16. R. G. Loucks, R. M. Reed, S. C. Ruppel and D. M. Jarvie, *J. Sediment. Res.*, 2009, **79**, 848-861.
17. L. Fu, S. Merabia and L. Joly, *Phys. Rev. Lett.*, 2017, **119**, 214501.
18. L. Joly, C. Ybert, E. Trizac and L. Bocquet, *Phys. Rev. Lett.*, 2004, **93**, 257805.
19. Y. Xie, L. Fu, T. Niehaus and L. Joly, *Phys. Rev. Lett.*, 2020, **125**, 014501.
20. M. Barisik and A. Beskok, *Phys. Fluids*, 2014, **26**, 052003.
21. G. E. Karniadakis, A. Beskok and N. Aluru, *Microflows and Nanoflows: Fundamentals and Simulation*, Springer, New York, 2005.
22. Z. Zhu, C. Fang, R. Qiao, X. Yin and E. Ozkan, *SPE Journal*, 2020, SPE-196136-PA, DOI:196110.192118/196136-PA.

23. S. W. I. Siu, K. Pluhackova and R. A. Böckmann, *J. Chem. Theory Comput.*, 2012, **8**, 1459-1470.
24. J. J. Potoff and J. I. Siepmann, *AIChE J.*, 2001, **47**, 1676-1682.
25. A. Rahaman, V. H. Grassian and C. J. Margulis, *J. Phys. Chem. C*, 2008, **112**, 2109-2115.
26. B. Hess, C. Kutzner, D. van der Spoel and E. Lindahl, *J. Chem. Theory Comput.*, 2008, **4**, 435-447.
27. R. Qiao and N. R. Aluru, *J. Chem. Phys.*, 2003, **118**, 4692-4701.
28. L. Martínez, R. Andrade, E. G. Birgin and J. M. Martínez, *J. Comput. Chem.*, 2009, **30**, 2157-2164.
29. R. Qiao and N. R. Aluru, *Int. J. Multiscale Comput. Eng.*, 2004, **2**, 16.
30. R. Bhadauria and N. R. Aluru, *J. Chem. Phys.*, 2017, **146**, 184106.
31. R. Bhadauria and N. R. Aluru, *J. Chem. Phys.*, 2013, **139**, 074109.
32. A. Iino, T. Onishi and A. Datta-Gupta, *SPE Reservoir Evaluation & Engineering*, 2020, **23**, 261-281.
33. A. Schlaich, J. Kappler and R. R. Netz, *Nano Lett.*, 2017, **17**, 5969-5976.
34. J. Koplik and J. R. Banavar, *Phys. Rev. Lett.*, 2006, **96**, 044505.